

# SEELE: A Unified Acceleration Framework for Real-Time Gaussian Splatting

Xiaotong Huang<sup>1\*</sup> He Zhu<sup>1\*</sup> Zihan Liu<sup>12</sup> Weikai Lin<sup>3</sup> Xiaohong Liu<sup>1</sup> Zhezhi He<sup>1</sup>  
Jingwen Leng<sup>12</sup> Minyi Guo<sup>12</sup> Yu Feng<sup>1†</sup>

<sup>1</sup>Shanghai Jiao Tong University <sup>2</sup>Shanghai Qi Zhi Institute <sup>3</sup>University of Rochester

Project Page: <http://seele-project.netlify.app>



Fig. 1. Our acceleration framework, SEELE, can be generalized to 3DGS algorithms, and achieves up to  $4\times$  speedup with superior rendering quality ( $> 0.5\text{dB}$ ) against the state-of-the-art 3DGS algorithms [15, 16, 20, 27, 32]. On a mobile Nvidia AGX Orin, SEELE achieves over 90 FPS (real-time requirement for VR). Meanwhile, SEELE maintains great portability with  $2.5\times$  speedup across GPU platforms (Tbl. 2).

## Abstract

3D Gaussian Splatting (3DGS) has become a crucial rendering technique for many real-time applications. However, the limited hardware resources on today’s mobile platforms hinder these applications, as they struggle to achieve real-time performance. In this paper, we propose SEELE, a general framework designed to accelerate the 3DGS pipeline for resource-constrained mobile devices.

Specifically, we propose two GPU-oriented techniques: hybrid preprocessing and contribution-aware rasterization. Hybrid preprocessing alleviates the GPU compute and memory pressure by reducing the number of irrelevant Gaussians during rendering. The key is to combine our view-dependent scene representation with online filtering. Meanwhile, contribution-aware rasterization improves the GPU utilization at the rasterization stage by prioritizing Gaussians with high contributions while reducing computations for those with low contributions. Both techniques can be seamlessly integrated into existing 3DGS pipelines with minimal fine-tuning. Collectively, our framework achieves

$2.6\times$  speedup and 32.3% model reduction while achieving superior rendering quality compared to existing methods.

## 1. Introduction

3D Gaussian Splatting (3DGS) [27] has emerged as a vital technique in many rendering-related domains, including autonomous driving [28, 35, 36, 42], augmented and virtual reality (AR/VR) [14, 24, 26, 41]. These real-time applications require high rendering performance to ensure seamless quality of services. However, the limited computational resources of mobile platforms often constrain these applications, preventing them from reaching their full potential.

For instance, Nvidia AGX Orin [6], a leading-edge compute module for modern vehicles, offers only 3.4% of the computational resources of a Nvidia A100 workstation GPU [2]. Similarly, the Snapdragon XR2 chip [8, 10], the most widely used chip for AR/VR devices, has 4.2% of the computational power compared to Nvidia RTX 4090 [1]. On Nvidia’s AGX Orin, 3DGS [27] merely achieves 20 FPS on real-world datasets [13, 23, 30], far from the real-time requirement, i.e., 90 frame-per-second (FPS) of VR and gam-

\*Equal contribution.

†Corresponding author.

ing [7, 9, 43]. An interesting challenge is to achieve real-time performance on these devices with only 3-4% of the compute resources compared to high-end GPUs.

To achieve this goal, we must understand the major performance bottlenecks in the current 3DGS rendering pipelines. We summarized the bottlenecks into three aspects: computational intensity, rendering inefficiency, and memory budget. This paper proposes a *one-stop solution* framework, SEELE<sup>\*</sup>, that addresses the inefficiencies across these three dimensions (Sec. 3). Next, we briefly discuss the inefficiencies in today’s 3DGS rendering pipeline and highlight how SEELE addresses these limitations.

**Computational Intensity.** One primary challenge in the 3DGS pipeline is its computational intensity. From an individual pixel’s perspective, rendering one pixel typically involves processing thousands of Gaussian points<sup>†</sup>, with each GPU thread rendering one pixel. This rendering process imposes substantial computational overhead on resource-constrained devices. Existing solutions [15, 16, 37] primarily focus on reducing the overall model size, namely the number of Gaussian points, but these methods often trade off rendering quality for performance.

In contrast, we propose *hybrid preprocessing* with a view-dependent scene representation that dynamically loads the relevant Gaussians to GPU memory during runtime (Sec. 4). Our data representation naturally identifies the necessary Gaussians contributing to the current viewpoint while leaving other irrelevant Gaussians untouched. Meanwhile, our method does not make any compromise between performance and accuracy. On average, this method alone outperforms the state-of-the-art rendering algorithms while achieving a  $2.1\times$  speedup.

**Rendering Inefficiency.** The second issue with the current 3DGS rendering pipeline is that all splatted Gaussians go through the same rasterization pipeline regardless of their contribution to the final pixels. Our experiment shows that, for each pixel, 1.5% of the Gaussians contribute to 99% of the final pixel. Therefore, we argue that this uniform treatment to all Gaussians leads to severe rendering inefficiencies, as *less significant Gaussians should naturally receive fewer computational budgets*. However, prior work [20, 32, 33], such as pruning or quantization techniques, still retains a uniform rendering pipeline and fails to differentiate Gaussians based on their contributions.

On the contrary, we propose contribution-aware rasterization from a pixel-centric perspective (Sec. 5). Rather than reducing computation uniformly, we dynamically identify and prioritize Gaussians with high contributions (i.e., high

accumulative transparencies) and reduce computation budgets for those with low contributions. Gaussians with low contributions, which typically contribute to low-frequency textures (as shown in Fig. 4), are allocated less computation by dynamically skipping insignificant operations. We show that this method achieves an additional  $1.3\times$  speedup while retaining the same rendering quality.

**Memory Budget.** Our last contribution eases the peak GPU memory. As model complexity scales up, the GPU memory requirements often become unsustainable due to the increasing number of Gaussians involved. Current solutions [32, 40] apply offline compression techniques to reduce memory usage, but they overlook a key opportunity: rendering a given viewpoint does not require loading all Gaussians into GPU memory simultaneously.

Leveraging this key observation, we design proactive memory management that asynchronously loads necessary data to GPU memory without disrupting the critical path of rendering. Combined with our view-dependent scene representation, our memory management significantly reduces peak GPU memory usage. On average, our approach achieves a 32.3% reduction in model size, allowing large-scale rendering on mobile devices.

Collectively, our framework achieves  $2.6\times$  speedup and 32.3% runtime model reductions, all while retaining a better rendering quality compared to state-of-the-art algorithms. Furthermore, our techniques are orthogonal to existing optimizations and can be seamlessly integrated with other mainstream Gaussian splatting pipelines.

The contribution of this paper is summarized as follows:

- We introduce a view-dependent scene representation that combines online and offline filtering to reduce computation overhead and runtime GPU memory.
- We propose a contribution-aware rasterization algorithm that dynamically skips the insignificant computations and improves the parallel efficiency.
- We design an integrated co-training procedure that integrates the aforementioned techniques and achieves better rendering quality against the corresponding baselines.

## 2. Related Work

### 2.1. Efficient Data Representation

A 3DGS model is essentially a set of points in 3D space that represent the physical structure of the world. The model size often becomes one of the key bottlenecks in rendering performance and memory usage. To reduce the model size, several studies have proposed various data representations to optimize storage and performance [15, 16, 20, 32, 39]. Some reduce GPU memory usage by leveraging encoding techniques to compress the model. For example, CompactGS [32] employs vector quantization to compress the model offline and decodes it at runtime using a pretrained

<sup>\*</sup>The name is an organization that comes from a famous Japanese anime, *Neon Genesis Evangelion*. This organization’s mission is to accomplish the Human Instrumentality Project. Similarly, the goal of our project is to address and resolve all the performance bottlenecks in 3DGS.

<sup>†</sup>We use “Gaussians”, “Gaussian points”, and “Gaussian ellipsoid” interchangeably: there is a one-to-one mapping between them.



codebook. Similarly, EAGLES [20] uses an encoding network to compress the neural radiance field into a compact representation. However, both methods introduce non-trivial execution overhead during runtime, which can limit their applicability in computation-constrained scenarios.

Other approaches, such as LightGaussian[15], Mini-Splatting[16], and Taming3DGS [37], propose various pruning techniques to eliminate insignificant Gaussians. However, these methods have to make a trade-off between rendering quality and efficiency. Some studies adopt structured data representations, such as octrees [40] and kd-tree [28], to organize Gaussian points more effectively. However, the irregular tree traversals required by these structures introduce additional runtime overhead.

In contrast to prior studies, we focus on real-time performance. Our view-dependent scene representation achieves significant model size reduction with minimal runtime overhead and no quality compromise.

## 2.2. Rasterization Optimization

In addition to pruning Gaussian points, another line of research focuses on optimizing the performance of the 3DGS pipeline itself. Recent studies propose various on-line filtering techniques, such as axis-aligned bounding box (AABB) [29, 44] and oriented bounding box (OBB) [21, 31] intersection tests, to perform more fine-grained filtering before rasterization. These works aim to reduce the number of Gaussians processed during the rasterization stage at runtime, thereby reducing the computational workload.

On the other hand, methods like FlashGS [17] and Balanced3DGS [22] focus on optimizing the rasterization stage. For example, FlashGS designs a software pipelining to overlap data fetching with rasterization, improving overall efficiency. In contrast, Balanced3DGS addresses workload imbalance by introducing an offline scheduling mechanism to rebalance workloads at both the block and tile levels. Additionally, a few studies [18, 31, 34] explore the new hardware designs to support 3DGS, further advancing the efficiency and scalability of the pipeline.

Unlike prior works, our optimization takes a unique angle to accelerate 3DGS by addressing the inherent contribution imbalance across Gaussian points. Our method dynamically assigns computational budgets to Gaussians based on their contributions to the final rendered image. Moreover, our algorithm is naturally GPU-friendly and alleviates execution inefficiencies such as warp divergence, achieving better overall performance with no hardware modifications.

## 3. SEELE Framework

### 3.1. Preliminaries

3DGS algorithms adhere to an explicit point-based representation, where each point is modeled by a Gaussian ellip-

soid (a.k.a., Gaussian for short) that captures the geometric and textural properties of the scene. The geometric property of a Gaussian is governed by its 3D centroid position  $x$  and a 3D covariance matrix  $\Sigma$ . The textural properties are described by two components: its opacity  $\sigma$  and spherical harmonic (SH) coefficients. Using these properties, the 3DGS pipeline renders a frame on a tile-by-tile basis via three steps: *preprocessing*, *sorting*, and *rasterization*.

**Preprocessing.** Given a camera pose and a view direction, the preprocessing stage first filters out Gaussians outside the current view frustum. Meanwhile, this stage identifies the intersection between Gaussians and rendering tiles.

**Sorting.** Once each tile collects its intersected Gaussians, the sorting stage determines the rendering order of those Gaussians. This stage ensures that all points are rendered, from the closest to the furthest, based on their depth.

**Rasterization.** Once all Gaussians are sorted, the rasterization stage renders these Gaussians tile-by-tile. Within each tile, every pixel iterates through the same set of Gaussians, computing transparency and accumulating their colors into the pixel in the sorted order. Eqn. 1 governs the color accumulation process of pixel  $\mathbf{p}$ :

$$C(\mathbf{p}) = \sum_{i=1}^N \Gamma_i \alpha_i \mathbf{c}_i, \text{ where } \Gamma_i = \prod_{j=1}^{i-1} (1 - \alpha_j) \quad (1)$$

where  $\Gamma_i$  denotes the accumulative transmittance of pixel  $\mathbf{p}$  from the Gaussian 1st to the  $i - 1$ th.  $\alpha_i$  and  $\mathbf{c}_i$  stand for the transparency and the color at the  $i$ th Gaussian, respectively. The transparency of a Gaussian  $\alpha_i$  is calculated by the Gaussian opacity  $\sigma_i$  and the 2D covariance matrix [45].  $\mathbf{c}_i$  is a function of the Gaussian’s spherical harmonics.

Note that, if the Gaussian’s  $\alpha_i$  value is insignificant (less than  $\alpha_\theta$ , i.e.,  $\frac{1}{255}$ ), this Gaussian will be skipped in the color accumulation to avoid numerical instabilities. The color accumulation process terminates once the accumulative transmittance  $\Gamma_i$  surpasses a predefined threshold,  $\Gamma_\theta$ .

### 3.2. Overview

Fig. 2 gives the overview of our acceleration framework, SEELE. To address three rendering inefficiencies highlighted in Sec. 1, we introduce two key components: *hybrid preprocessing* and *contribution-aware rasterization* to reduce the runtime computation and peak memory.

In 3DGS pipelines, rasterization is the most time-consuming stage, accounting for  $>67\%$  of the execution time on a Nvidia Ampere GPU [6]. Prior studies have explored two primary methods to reduce the overall workload of rasterization. The first approach applies pruning techniques, which eliminate insignificant Gaussians offline [15, 16]. The second proposes online filtering techniques, such as AABB and OBB intersection tests, to perform more fine-grained filtering before rasterization [21, 29, 31, 44].

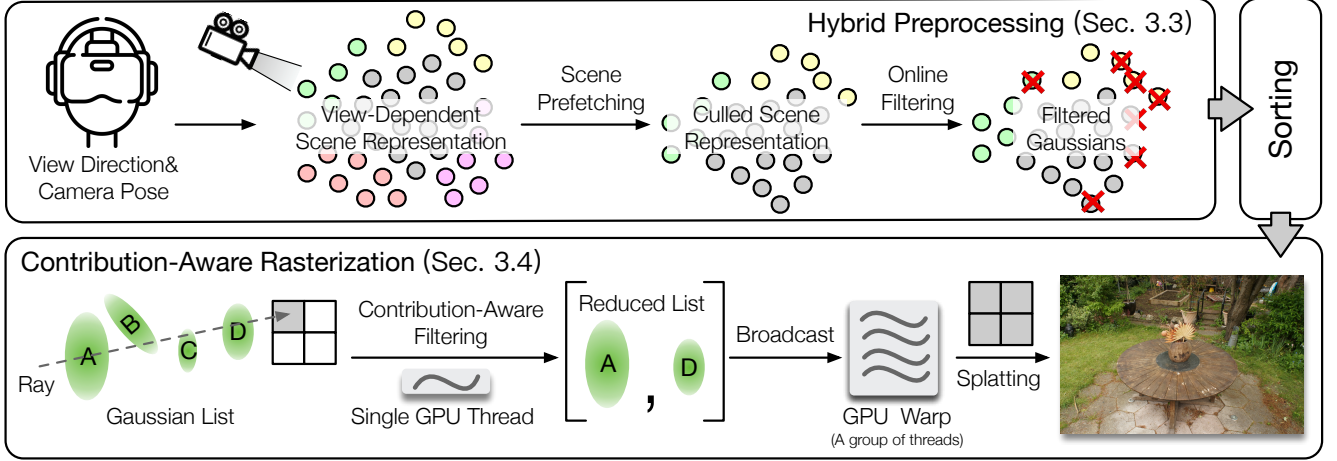


Fig. 2. SEELE modifies the two steps, *preprocessing* and *rasterization*, and proposes two novel techniques: *hybrid preprocessing* and *contribution-aware rasterization*, in Gaussian splatting. Hybrid preprocessing leverages offline coarse-grained scene clustering and online filtering to reduce the number of Gaussians before rasterization. Contribution-aware rasterization dynamically identifies insignificant Gaussian and skips the rasterization of those Gaussian to accelerate the overall rendering pipeline with even better rendering quality.

Our hybrid preprocessing combines the merits of both offline and online techniques. During the offline processing, we design a view-dependent scene representation that clusters Gaussians based on their contributions to a set of closely related rendering viewpoints. At runtime, our framework can asynchronously prefetch the relevant clusters into the GPU memory before rendering. This approach largely reduces the filtering workload during preprocessing. In addition, the view-dependent scene representation inherently eliminates Gaussians that are irrelevant to current rendering while within the view frustum. Combined with online filtering, our hybrid preprocessing collectively minimizes the processed Gaussians in rasterization.

Meanwhile, we propose a novel contribution-aware rasterization to accelerate the rasterization pipeline itself. The key idea of our approach is to penalize the computations assigned to insignificant Gaussians purposely, allowing for efficient rendering without compromising quality.

Specifically, our rasterization pipeline organizes pixels into small groups while still keeping one thread responsible for one pixel. At runtime, only a single pixel within each pixel group calculates its Gaussian transparency  $\alpha$  rather than having all pixels compute  $\alpha$ . The purpose is to let this pixel identify Gaussians that potentially contribute less to the pixel group. Since the identified Gaussians are likely to have minimal impact on the remaining pixels within a pixel group, we exclude these Gaussians from further rasterization. In this way, we eliminate insignificant Gaussian accumulation at runtime. Combined with our integrated co-training, we can achieve even better rendering quality.

In the next two sections, we will introduce our two techniques, *hybrid preprocessing* (Sec. 4) and *contribution-*

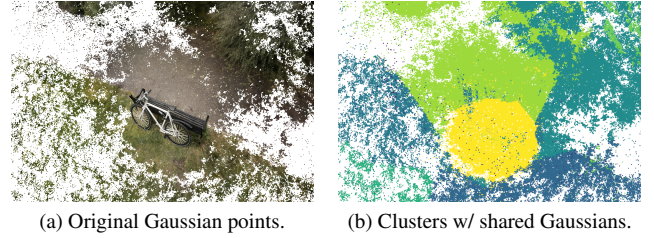


Fig. 3. Our scene representation clusters all Gaussians into shared Gaussians and exclusive Gaussians. Here, we show the Gaussian positions *without* scales. The yellow points in Fig. 3b represent the shared Gaussians, while the remaining colored points correspond to the exclusive Gaussians in different clusters.

*aware rasterization* (Sec. 4), in detail.

## 4. Hybrid Preprocessing, HP

**View-Dependent Scene Representation.** The idea of this data representation is to preprocess Gaussians offline, thereby reducing computational effort during the online preprocessing stage. Our key observation is that different viewpoints rely on distinct sets of Gaussians for rendering. Viewpoints in close proximity are likely to share similar Gaussians, while those farther apart share fewer.

Based on this observation, our data representation classifies Gaussians into two categories: shared Gaussians and exclusive Gaussians, as shown in Fig. 3. Shared Gaussians are shared across all viewpoints and are frequently used for rendering frames from any viewpoint. On the other hand, exclusive Gaussians are specifically attached to a group of viewpoints and are only used for rendering frames within that group. For instance, Fig. 3a illustrates the original set

of Gaussian points, which are then clustered as shown in Fig. 3b. The yellow points in Fig. 3b represent the shared Gaussians, while the remaining colored points correspond to the exclusive Gaussians in different clusters.

**Clustering Strategy.** The key to our approach lies in how to classify the Gaussians into shared and exclusive Gaussians. Initially, our method randomly samples camera poses and clusters them into  $N$  smaller groups based on the weighted similarity of their camera positions,  $\vec{x}$  and view directions,  $\vec{v}$ . Specifically, we first normalize the camera positions,  $\vec{x}$ , then concatenate normalized  $\vec{x}$  and  $\vec{v}$  as a 1D dimensional vector,  $(\vec{x}, \beta\vec{v})$ , where  $\beta$  is a hyperparameter that balances the impact of position and orientation.  $(\vec{x}, \beta\vec{v})$  is used to cluster all Gaussians.

For each cluster, we identify and reserve the Gaussians that are the primary contributors to pixel rendering. Specifically, for each pixel, we find the Top- $k$  Gaussians based on their contribution to the accumulative transmittance,  $\Gamma_i\alpha_i$ , as the contribution metric. The rationale here is that the remaining Gaussians contribute minimally to the final pixel and can be safely discarded without compromising rendering quality. We empirically choose a  $k$  value of 32, as we find that increasing  $k$  further does not yield any significant improvement in rendering quality.

Once we identify the top Gaussian contributors for each cluster, we find the union of top contributors across all clusters and grant these top Gaussians to be shared across all clusters. These granted Gaussians are then the shared Gaussians in our representation. The remaining Gaussians within each cluster are classified as exclusive Gaussians.

**Algorithm.** During the actual rendering, for a given camera pose, our approach first identifies the nearest cluster based on the cluster centroid. Next, all Gaussians belonging to this cluster and its  $M$  neighboring clusters are selected, as shown in Fig. 2. In this example, green points are the nearest cluster, and the yellow points are the nearest neighbors to that cluster ( $M$  is set to 1 in this toy example). The selected  $1 + M$  clusters are used to render the current camera pose instead of all Gaussians. Note that, shared Gaussians, gray points in Fig. 2, are always stored in GPU memory since they are used for any poses. Unlike the original 3DGS, our approach retains only the relevant clusters to stay in GPU memory, thus reducing the peak GPU memory usage. Empirically, we set  $M$  to be 3, which strikes a good balance between performance and rendering quality.

Once these Gaussians are loaded, we incorporate this coarse-grained scene prefetching with fine-grained online filtering, e.g., AABB tests, as shown in Fig. 2. This further eliminates false-positive intersected Gaussians when performing Gaussian-tile intersections. The red crosses in Fig. 2 highlight the false-positive Gaussians. Sec. 7.3 shows the effectiveness of our hybrid preprocessing.

**Scene Prefetching.** Our hybrid preprocessing not only

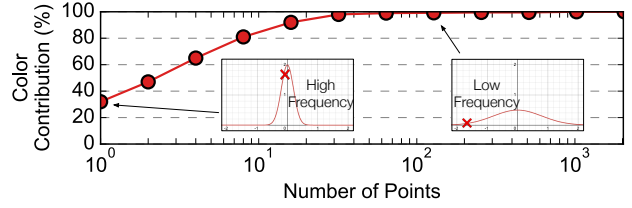


Fig. 4. The significance of Gaussians towards the final pixel. Gaussians are sorted in descending order. We empirically find that significant Gaussians are typically sampled in high-frequency regions, while insignificant Gaussians are more likely to be sampled in low-frequency regions, as shown by the red crosses.

enhances rendering performance but also reduces peak GPU memory usage. However, loading Gaussian clusters at runtime could introduce non-trivial execution overhead and potentially cause frame stalling. To address this, we prefetch future clusters ahead of time by asynchronously loading them using a dedicated GPU stream. We find that using linearly extrapolating the camera pose is an effective method for predicting future poses in our scene prefetching. We adopt similar prediction methods as prior works [19, 25] and claim no contribution to this end. This way, our approach enables asynchronous prefetching to be overlapped with runtime frame rendering. Compared to loading all Gaussian clusters into GPU memory, our scene prefetching strategy reduces the runtime model size by 32.27%.

## 5. Contribution-Aware Rasterization, CR

### 5.1. Algorithm

**Motivation.** The goal of our contribution-aware rasterization is to pay “computational” attention to significant Gaussians that contribute more to the final pixel values while reducing computations for less important Gaussians. Our observation is that the color values of most pixels are determined by a small fraction of Gaussians, as illustrated in Fig. 4. We characterize the MipNeRF360 dataset [13] and draw the accumulative transparency of each pixel by sorting the Gaussian transparency contribution  $\Gamma\alpha$  in descending order. The result in Fig. 4 shows that 1.5% of the top Gaussians contribute to 99% of the final pixel. The remaining Gaussians contribute minimally, primarily adding low-frequency textures. This is not an artifact but an inherent feature of Gaussian representation. Because low  $\alpha$  values are typically indicative of low-frequency information, whereas high  $\alpha$  values are often associated with high-frequency details, as shown by the red crosses in Fig. 4.

**Idea.** To leverage this observation, we propose a *contribution-aware rasterization* algorithm, as outlined in Algo. 1. Instead of uniformly assigning the same computation to all Gaussians, our algorithm organizes every  $w \times w$  pixels into small groups,  $P$ . During each iteration, only the

**Algorithm 1: Contribution-Aware Rasterization**

**Data:** a list of Gaussians  $G$ , a group of pixels  $P$   
**Result:** an image tile  $I$

```

1 I.init();
2 for  $g \in G$  do
3    $\alpha_0 \leftarrow \text{ComputeTransparency}(P[0], g)$ ;
4   if  $\alpha_0 < \alpha_\theta$  then
5     continue;
6   end
7   for  $p \in P$  do
8      $\alpha_{p,g} \leftarrow \text{ComputeTransparency}(p, g)$ ;
9      $I \leftarrow \text{AccumulateColor}(\alpha_{p,g}, p)$ ;
10  end
11  CheckTermination();
12 end

```

leader pixel  $p$  within a group, which is the centroid of this group, computes the  $\alpha$  value for a given Gaussian,  $g$ . If this  $\alpha$  value falls below a predefined threshold  $\alpha_\theta$  ( $\frac{1}{255}$ , to avoid numerical instability), the algorithm skips the color blending of this Gaussian on the remaining pixels within the group,  $P$ . This selective skipping largely reduces the workload for less important Gaussians.

For Gaussians deemed important (i.e., those with  $\alpha$  values above the threshold,  $\alpha_\theta$ ), our algorithm performs the same rasterization computations as the original approach, ensuring rendering quality is preserved. This dynamic computation reassignment improves rendering efficiency without compromising visual quality.

**GPU Parallelism.** Not only does our algorithm reduce the overall computation, but it also inherently achieves higher parallelism by alleviating warp divergence. In the GPU implementation, pixels within a group are assigned to one warp. All pixels within a warp execute in “lockstep” as shown in Fig. 7. For instance, when blending Gaussian  $A$ , only thread 1 accumulates the insignificant Gaussian  $A$  into its pixel, while all other threads are masked by GPU and wait for thread 1 to complete.

In contrast, our algorithm only lets thread 0 detect if Gaussian  $A$  is insignificant. In this case, all threads in this warp skip the color blending of Gaussian  $A$ . In the case of Gaussian  $B$ , because it is considered significant, all threads would blend Gaussian  $B$  instead. This ensures that these pixels either skip or process the same Gaussians collectively. This way, we eliminate branching within a warp.

## 5.2. Memory Optimization

In our *contribution-aware rasterization*, we further introduce a fine-grained pipelining that overlaps computation with data fetching from GPU memory to shared memory.

**Double Buffering.** Fig. 5 illustrates a simplified GPU

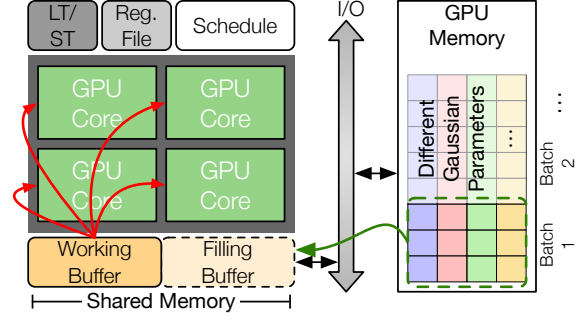


Fig. 5. A toy example of applying double buffering with a single streaming multiprocessor (SM). The shared memory of this SM is split into a working buffer and a filling buffer. The working buffer provides the data for processing the current batch, while the filling buffer loads the data from GPU memory for the next batch.

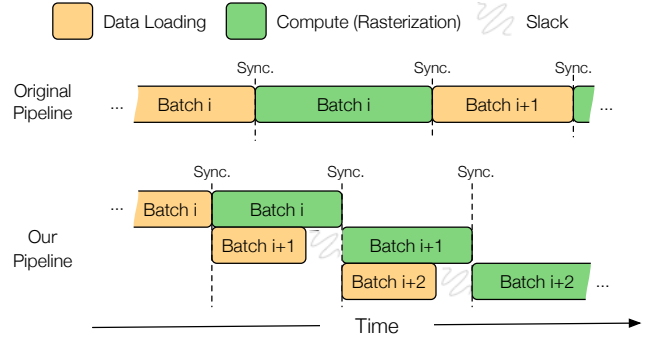


Fig. 6. The comparison between the original pipeline and our fine-grained pipelining. Our pipeline leverages the double buffering in shared memory and avoids the extra synchronization between data loading and computation. In our pipeline, we only need to synchronize between two compute batches.

design with our double buffering strategy. Specifically, it shows a streaming multiprocessor (SM), in Nvidia’s terminology, which consists of multiple compute cores. Each SM includes several GPU cores and a shared memory, a relatively small on-chip buffer (32-64 KB) for faster data access. Compared to accessing GPU memory, reading data from shared memory is often much faster. Note that, we intentionally ignore other buffers, e.g., L2 caches, in the GPU memory hierarchy to keep the illustration simple.

Our double buffering strategy splits the shared memory into two buffers: a working buffer and a filling buffer. The filling buffer preloads data for the next batch of computations, while the working buffer stores the data required for the current batch. In Fig. 5, the red arrows show that different GPU cores access data from the working buffer for their own computations. Meanwhile, as the green arrow shows, the filling buffer fetches data from GPU memory, preparing for the next batch of computations.

**Fine-Grained Pipelining.** With our double buffer-



ing strategy, the rasterization pipeline achieves a more fine-grained pipelining compared to the conventional rasterization pipeline in canonical Gaussian splatting. Fig. 6 provides a simplified example of rendering frames within a single warp. In the original algorithm, data loading and computing (rasterization) have to execute sequentially due to the warp-level synchronization. The on-chip data need to be synchronized to ensure the rendering’s correctness. However, the synchronization after compute batch unnecessary since there is no data dependency between computing the current batch and loading data for the next batch. This unnecessary synchronization is because the entire shared memory is allocated to a single batch of computation, forcing synchronization after each batch.

Thus, our pipeline partitions shared memory, allocating only half for each batch of computation. This allows data to be loaded into the second half while the current batch is being processed, as illustrated in Fig. 6.

Specifically, each warp loads the attributes of two Gaussians, with each thread within a warp loading one byte of the Gaussian attributes. A single GPU block, which consists of 8 warps, effectively loads 16 Gaussian points into shared memory. Here, we intentionally keep the batch size small to achieve finer-grained pipelining. For more details on the implementation, please refer to our code, which will be made available upon acceptance of this work.

## 6. Integrated Fine-Tuning

Note that, both HP and CR modify the rendering pipeline. To regain the rendering quality, our algorithm only requires minimal fine-tuning to achieve better rendering quality. Since both *hybrid preprocessing* and *contribution-aware rasterization* do not participate in gradient descent, these two techniques can be integrated into the current training process without any notifications on back-propagation.

Once the 3DGS model is trained by the canonical training process, we convert the model into our view-dependent scene representation as described in Sec. 4. Next, we fix the shared Gaussians and fine-tune only the exclusive Gaussians in each cluster individually for 1000 steps. Since our algorithm always takes  $1 + M$  clusters (1 nearest cluster and  $M$  neighboring clusters) during rendering, it naturally accommodates the view discrepancies when shifting between two cluster boundaries. Lastly, we fix the exclusive Gaussians and fine-tune the shared ones for 1000 steps.

## 7. Evaluation

### 7.1. Experimental Setup

**Code Optimization.** In addition to the two proposed techniques in Sec. 3, we also implement the following optimizations. First, we apply fine-grained data fetching when loading Gaussian attributes to better utilize shared memory on

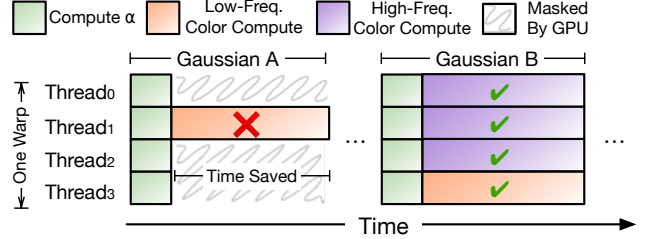


Fig. 7. An example of warp divergence in GPU. All threads compute  $\alpha$  and then perform color blending in “lockstep”. Our algorithm can detect the insignificant Gaussians (e.g., Gaussian A) and skip their color blending, as highlighted by the red cross. Thus, we save the total execution time.

GPU. Second, we leverage thread-level parallelism to overlap the execution of fetching Gaussian attributes and computation of alpha blending. Lastly, we replace the compute-intensive  $\exp()$  function with CUDA intrinsic function  $\_exp()$ , which generates fewer machine instructions once compiled. Note that, all optimizations above are nothing more than engineering hacks to improve the program’s efficiency; we do not claim them as our major contributions.

**Dataset and Metrics.** SEELE is evaluated on three datasets: Mip-NeRF360 [13], Tank&Temple [30], and DeepBlending [23]. For quality evaluation, we use PSNR, SSIM, and LPIPS. We also report frame-per-second (FPS), the number of executed instructions (#Inst.), and the runtime model size as our performance metrics.

**Baselines.** To show the general applicability of our optimization technique, we apply our framework to three state-of-the-art 3DGS algorithms: 3DGS [27], MiniSplatting [16], and LightGaussian [15].

**Algorithm Configurations.** Unless specified otherwise, we set the number of clusters to be 24 and fix the nearest neighbor cluster,  $M$ , to be 4 in Sec. 4. The pixel group,  $P$ , is set to  $2 \times 2$  in Sec. 5.

**Hardware.** The primary hardware we used is a mobile Ampere GPU on Nvidia AGX Orin SoC, which is the flagship development board in AR/VR and autonomous driving. Meanwhile, we also report the performance numbers on Nvidia Orin NX [5], a low-power embedded computing board, and Nvidia A6000 [3], a powerful workstation GPU.

### 7.2. Performance and Quality

**Quality Evaluation.** Tbl. 1 shows the overall evaluation of SEELE on three widely-used 3DGS pipelines: 3DGS [27], MiniSplatting [16], and LightGaussian [15]. Overall, SEELE generally achieves better rendering quality on all three datasets across all three evaluation metrics. For instance, on average, SEELE improves PSNR and SSIM by 0.28 dB and 0.004, respectively. Fig. 10 and Fig. 11 show the examples of the qualitative comparison between SEELE

Table 1. Quantitative evaluation of our method against the state-of-the-arts [15, 16, 20, 27, 32, 43]. The **green bold** results highlight the better results between ours, SEELE, and the corresponding baselines. SEELE achieves better quality across all three quality metrics with an average  $2.56\times$  speedup. ① and ② denote the **best** and **second-best** results among all methods, respectively.

Dataset	Mip-NeRF360						Tanks&Temples						Deep Blending					
Metrics	PSNR $\uparrow$	Quality SSIM $\uparrow$	LPIPS $\downarrow$	FPS $\uparrow$	Efficiency #Inst.(10 <sup>6</sup> ) $\downarrow$	Mem.(MB) $\downarrow$	PSNR $\uparrow$	Quality SSIM $\uparrow$	LPIPS $\downarrow$	FPS $\uparrow$	Efficiency #Inst.(10 <sup>6</sup> ) $\downarrow$	Mem.(MB) $\downarrow$	PSNR $\uparrow$	Quality SSIM $\uparrow$	LPIPS $\downarrow$	FPS $\uparrow$	Efficiency #Inst.(10 <sup>6</sup> ) $\downarrow$	Mem.(MB) $\downarrow$
CompactGS [32]	26.99	0.797	0.247	24.18	1824.57	122.7	23.42	0.831	0.202	46.53	920.04	93.0	29.84	0.902	0.257	32.87	1294.45	104.0
EAGLES [20]	27.14	0.805	0.239	22.30	1988.56	68.1	23.34	0.836	0.200	60.27	713.29	34.0	29.95	0.907	0.249	25.24	1555.53	61.5
AdR-Gaussian [44]	26.90	0.783	0.272	65.95	885.27	274.3	23.53	0.832	0.205	114.18	442.99	192.0	29.65	0.901	0.254	78.87	485.00	335.5
3DGS [27]	27.46	0.812	0.223	20.79	2168.68	710.6	23.75	0.848	0.176	41.97	1034.37	430.9	29.59	0.902	0.244	23.94	1645.11	639.9
SEELE + 3DGS	② <b>27.70</b>	② <b>0.814</b>	② <b>0.219</b>	<b>59.69</b>	<b>778.25</b>	<b>380.9</b>	② <b>24.02</b>	② <b>0.852</b>	② <b>0.168</b>	<b>128.34</b>	<b>356.15</b>	<b>207.6</b>	<b>29.79</b>	<b>0.903</b>	② <b>0.240</b>	<b>84.98</b>	<b>421.74</b>	<b>400.6</b>
MiniSplatting [16]	27.23	0.814	0.222	71.31	797.96	145.7	23.18	0.837	0.187	143.27	329.69	83.3	② <b>30.04</b>	② <b>0.908</b>	0.243	120.01	382.86	154.9
SEELE + MiniSplatting	② <b>27.70</b>	② <b>0.822</b>	② <b>0.212</b>	<b>131.62</b>	<b>436.41</b>	<b>106.5</b>	<b>23.74</b>	② <b>0.846</b>	② <b>0.179</b>	<b>268.03</b>	<b>172.40</b>	<b>60.1</b>	② <b>30.02</b>	② <b>0.908</b>	② <b>0.242</b>	<b>200.62</b>	<b>224.58</b>	<b>129.6</b>
LightGaussian [15]	27.44	0.807	0.235	30.89	1533.50	⑤ 59.4	23.82	0.842	0.189	65.60	699.71	③ 33.8	<b>29.74</b>	<b>0.901</b>	0.250	43.17	1097.82	⑤ 52.4
SEELE + LightGaussian	<b>27.56</b>	<b>0.810</b>	<b>0.229</b>	② <b>76.36</b>	② <b>589.85</b>	③ <b>39.1</b>	② <b>23.91</b>	<b>0.846</b>	<b>0.181</b>	<b>197.94</b>	② <b>259.78</b>	<b>20.7</b>	29.73	0.900	<b>0.249</b>	② <b>114.02</b>	② <b>324.25</b>	② <b>41.4</b>

and its corresponding baselines. Visually, there is no quality difference between SEELE and the corresponding baselines.

**Performance Evaluation.** SEELE consistently achieves speedups across all algorithms. On average, SEELE achieves  $3.2\times$ ,  $1.8\times$ , and  $2.7\times$  speedup on 3DGS, MiniSplatting and LightGaussian, respectively. The higher speedup observed in 3DGS compared to the other two algorithms can be attributed to the denser nature of 3DGS. This density allows SEELE to better separate irrelevant Gaussians contributed to different views using *hybrid preprocessing* introduced in Sec. 4, resulting in greater speedup. Despite that, sparse models like MiniSplatting still benefit from *hybrid preprocessing* due to the view-dependent redundancy, i.e., different views require different Gaussians to render. Tbl. 1 also shows the average number of executed instructions of each algorithm using NVIDIA Nsight Compute [4], SEELE indeed reduces the overall computation. Tbl. 3 further dissects the contributions.

Tbl. 2 shows the speedup of SEELE on additional GPUs, Nvidia Orin NX and Nvidia A6000. The results show that the optimizations proposed in SEELE are not tied to a specific GPU architecture, exhibiting good generality across different hardware platforms. However, we observe that our optimization achieves a higher speedup on lower-power GPUs, as shown in Tbl. 2. For example, SEELE + 3DGS achieves a  $2.9\times$  speedup on the Orin NX, while it achieves a  $2.4\times$  speedup on the A6000. Primarily, it is because low-end GPUs often have restricted hardware resources, i.e., compute units, GPU bandwidth, etc.

SEELE not only speeds up the overall rendering process but also reduces overall GPU memory consumption. Here, we exclusively focus on the GPU memory contributed by the Gaussian points, i.e., runtime model weights. Overall, results show that SEELE achieves 32.3% reduction in runtime model size across three different datasets. Even for sparse models like MiniSplatting, SEELE still saves 23.2% of model size compared to the baselines.

### 7.3. Ablation Study

In this section, we show the contributions of individual optimizations. Specifically, we evaluate four variants:

- **+Opti.:** this variant only includes the additional code optimizations proposed in Sec. 7.1.
- **+Opti.+HP:** this variant includes both the code optimizations in Sec. 7.1 and *hybrid preprocessing* in Sec. 4.
- **+Opti.+CR:** this variant includes code optimizations in Sec. 7.1 and *contribution-aware rasterization* in Sec. 5.
- **SEELE:** this variant is the full-fledged algorithm including all optimizations proposed in this paper.

Tbl. 3 presents the results of our ablation study on 3DGS [27], MiniSplatting [16] and LightGaussian [15]. Across all datasets, our code optimization (**+opti.**) achieves a  $1.1\times$  speedup. Building on this, **+Opti.+HP** and **+Opti.+CR** yield additional  $2.8\times$  and  $1.3\times$  speedups, respectively. When all optimizations are combined, SEELE achieves an overall  $3.3\times$  speedup. All model weight savings come from HP, as the other two optimizations do not contribute to the model reduction. Note that, SEELE may increase the overall instruction count but improves the overall speedup due to the reductions on warp divergence.

In terms of the rendering quality, the additional optimizations proposed in Sec. 7.1 do not change the accuracy. The HP technique from Sec. 4, combined with fine-tuning as described in Sec. 6, further enhances rendering quality across all three quality metrics. On average, HP improves the rendering quality by 0.23 on PSNR. The effect of CR from Sec. 5 on quality is minimal, 0.03 in PSNR.

**Fine-Tuning.** Next, we present the results with and without the integrated fine-tuning, as described in Sec. 6. Here, we focus on the results of the Mip-NeRF360 dataset with 3DGS. Similar trends are observed across other datasets in the supplementary. As shown in Tbl. 4, incorporating fine-tuning results in significant improvements across all quality metrics. At the same time, fine-tuning does not affect performance, with both FPS and GPU memory consumption remaining relatively unchanged.

Table 2. Quantitative evaluation of our method against the recent works: 3DGS [27], MiniSplatting [16], and LightGaussian [15]. The **green bold** results highlight the better results between ours, SEELE, and the corresponding baselines.

Metrics	Method	Mip-NeRF360										Tanks&Temples		Deep Blending	
		Bicycle	Bonsai	Counter	Flowers	Garden	Kitchen	Room	Stump	Treehill		Train	Truck	Playroom	Drjohnson
PSNR↑	3DGS [27]	<b>25.11</b>	<b>32.20</b>	29.08	21.44	27.38	31.24	31.56	<b>26.70</b>	22.46		22.06	25.44	29.92	29.26
	SEELE + 3DGS	25.02	33.15	<b>29.60</b>	<b>21.50</b>	<b>27.45</b>	<b>31.67</b>	<b>32.04</b>	26.57	<b>22.49</b>		<b>22.39</b>	<b>25.65</b>	<b>30.11</b>	<b>29.48</b>
	MiniSplatting [16]	24.86	31.86	28.74	21.16	26.18	31.38	31.47	26.78	22.63		21.37	25.00	30.42	29.66
	SEELE + MiniSplatting	<b>25.21</b>	<b>32.86</b>	<b>29.31</b>	<b>21.38</b>	<b>26.96</b>	<b>32.11</b>	<b>31.69</b>	<b>26.97</b>	<b>22.79</b>		<b>22.02</b>	<b>25.46</b>	<b>30.37</b>	<b>29.67</b>
	LightGaussian [15]	<b>25.13</b>	32.20	28.98	21.41	27.01	31.14	31.87	<b>26.66</b>	22.53		22.16	25.47	30.03	<b>29.44</b>
	SEELE + LightGaussian	24.94	<b>32.72</b>	<b>29.32</b>	<b>21.44</b>	<b>27.06</b>	<b>31.43</b>	<b>32.03</b>	26.52	<b>22.54</b>		<b>22.30</b>	<b>25.52</b>	<b>30.03</b>	29.43
SSIM↑	3DGS [27]	0.745	0.945	0.915	0.589	0.857	0.931	0.927	<b>0.768</b>	0.634		0.817	0.879	0.902	0.902
	SEELE + 3DGS	<b>0.745</b>	<b>0.950</b>	<b>0.919</b>	<b>0.593</b>	<b>0.858</b>	<b>0.934</b>	<b>0.929</b>	0.765	<b>0.634</b>		<b>0.821</b>	<b>0.882</b>	<b>0.903</b>	<b>0.903</b>
	MiniSplatting [16]	0.750	0.948	0.913	0.592	0.827	0.932	0.930	0.787	0.649		0.803	0.872	0.908	0.908
	SEELE + MiniSplatting	<b>0.763</b>	<b>0.953</b>	<b>0.920</b>	<b>0.607</b>	<b>0.842</b>	<b>0.937</b>	<b>0.932</b>	<b>0.795</b>	<b>0.655</b>		<b>0.815</b>	<b>0.878</b>	<b>0.908</b>	<b>0.908</b>
	LightGaussian [15]	0.743	0.941	0.907	0.585	0.840	0.926	0.925	<b>0.769</b>	0.630		0.806	0.878	0.902	<b>0.899</b>
	SEELE + LightGaussian	<b>0.743</b>	<b>0.945</b>	<b>0.911</b>	<b>0.590</b>	<b>0.843</b>	<b>0.929</b>	<b>0.926</b>	0.767	<b>0.633</b>		<b>0.811</b>	<b>0.880</b>	<b>0.902</b>	0.898
LPIPS↓	3DGS [27]	0.245	0.181	0.183	0.359	0.124	0.118	0.197	0.245	0.347		0.203	0.148	0.247	0.241
	SEELE + 3DGS	<b>0.238</b>	<b>0.176</b>	<b>0.177</b>	<b>0.353</b>	<b>0.118</b>	<b>0.113</b>	<b>0.193</b>	<b>0.241</b>	<b>0.343</b>		<b>0.194</b>	<b>0.141</b>	<b>0.243</b>	<b>0.237</b>
	MiniSplatting [16]	0.256	0.166	0.176	0.353	0.171	0.115	0.184	0.237	0.344		0.223	0.150	0.245	0.240
	SEELE + MiniSplatting	<b>0.240</b>	<b>0.161</b>	<b>0.168</b>	<b>0.340</b>	<b>0.155</b>	<b>0.109</b>	<b>0.181</b>	<b>0.223</b>	<b>0.332</b>		<b>0.214</b>	<b>0.144</b>	<b>0.245</b>	<b>0.239</b>
	LightGaussian [15]	0.255	0.192	0.201	0.372	0.148	0.130	0.204	0.247	0.367		0.227	0.150	0.251	0.249
	SEELE + LightGaussian	<b>0.248</b>	<b>0.186</b>	<b>0.194</b>	<b>0.366</b>	<b>0.142</b>	<b>0.125</b>	<b>0.200</b>	<b>0.243</b>	<b>0.358</b>		<b>0.219</b>	<b>0.143</b>	<b>0.250</b>	<b>0.248</b>
FPS↑ on Orin	3DGS [27]	12.18	33.93	24.61	27.84	16.57	19.65	22.15	23.00	22.28		43.67	40.39	28.94	20.41
	SEELE + 3DGS	<b>40.15</b>	<b>98.47</b>	<b>67.76</b>	<b>71.91</b>	<b>46.83</b>	<b>54.63</b>	<b>86.06</b>	<b>45.00</b>	<b>68.86</b>		<b>139.28</b>	<b>118.08</b>	<b>93.38</b>	<b>80.70</b>
	MiniSplatting [16]	93.41	59.33	45.65	96.50	91.85	50.32	67.71	95.34	96.43		149.66	137.40	133.58	108.93
	SEELE + MiniSplatting	<b>176.80</b>	<b>116.21</b>	<b>89.38</b>	<b>177.59</b>	<b>162.34</b>	<b>88.62</b>	<b>121.36</b>	<b>161.34</b>	<b>184.57</b>		<b>264.27</b>	<b>271.89</b>	<b>233.54</b>	<b>175.84</b>
	LightGaussian [15]	18.71	43.64	35.29	41.92	28.43	29.11	29.01	36.43	31.90		74.57	58.57	51.89	36.96
	SEELE + LightGaussian	<b>61.43</b>	<b>102.4</b>	<b>81.44</b>	<b>88.65</b>	<b>62.33</b>	<b>69.09</b>	<b>75.58</b>	<b>80.80</b>	<b>82.33</b>		<b>209.73</b>	<b>163.67</b>	<b>143.35</b>	<b>120.88</b>
FPS↑ on Orin NX	3DGS [27]	1.74	5.03	3.46	4.35	2.53	2.73	3.23	3.59	3.33		6.34	5.75	4.50	3.06
	SEELE + 3DGS	<b>6.62</b>	<b>14.68</b>	<b>10.81</b>	<b>12.04</b>	<b>7.02</b>	<b>7.71</b>	<b>12.07</b>	<b>9.44</b>	<b>10.00</b>		<b>21.93</b>	<b>17.76</b>	<b>16.59</b>	<b>13.40</b>
	MiniSplatting [16]	9.32	8.05	6.16	10.01	10.26	6.82	8.88	10.36	10.32		21.68	19.57	18.76	15.28
	SEELE + MiniSplatting	<b>20.25</b>	<b>16.38</b>	<b>13.02</b>	<b>20.73</b>	<b>20.05</b>	<b>13.17</b>	<b>18.39</b>	<b>19.48</b>	<b>20.94</b>		<b>43.39</b>	<b>40.29</b>	<b>36.05</b>	<b>29.42</b>
	LightGaussian [15]	3.25	6.60	4.71	5.71	3.93	4.30	3.58	4.91	4.31		10.28	8.04	7.00	4.92
	SEELE + LightGaussian	<b>10.14</b>	<b>18.03</b>	<b>13.11</b>	<b>15.85</b>	<b>10.33</b>	<b>11.12</b>	<b>13.91</b>	<b>12.46</b>	<b>13.27</b>		<b>31.83</b>	<b>24.13</b>	<b>22.45</b>	<b>18.67</b>
FPS↑ on A6000	3DGS [27]	78.47	212.49	147.78	186.60	107.79	123.18	142.96	160.67	148.65		190.77	204.83	193.24	130.62
	SEELE + 3DGS	<b>217.39</b>	<b>499.75</b>	<b>401.61</b>	<b>398.57</b>	<b>233.92</b>	<b>289.02</b>	<b>449.64</b>	<b>336.36</b>	<b>353.98</b>		<b>573.72</b>	<b>504.29</b>	<b>556.79</b>	<b>480.08</b>
	MiniSplatting [16]	518.67	348.55	274.80	532.77	508.65	304.32	407.17	546.45	529.94		685.40	324.36	768.64	645.16
	SEELE + MiniSplatting	<b>809.72</b>	<b>558.97</b>	<b>464.90</b>	<b>798.08</b>	<b>720.46</b>	<b>478.47</b>	<b>640.61</b>	<b>725.16</b>	<b>824.40</b>		<b>1081.08</b>	<b>1137.66</b>	<b>1124.86</b>	<b>952.38</b>
	LightGaussian [15]	129.25	260.08	193.09	234.69	165.84	179.21	190.95	217.20	168.69		343.64	305.53	285.31	198.85
	SEELE + LightGaussian	<b>334.78</b>	<b>594.53</b>	<b>449.03</b>	<b>527.70</b>	<b>342.35</b>	<b>401.61</b>	<b>487.57</b>	<b>424.27</b>	<b>449.64</b>		<b>827.81</b>	<b>694.44</b>	<b>741.29</b>	<b>589.28</b>
#Inst.(10 <sup>6</sup> )↓	3DGS [27]	3333.20	1390.33	1948.76	1456.05	2607.93	2446.63	2668.26	1806.44	1860.57		944.96	1123.78	1212.77	2077.46
	SEELE + 3DGS	<b>1101.41</b>	<b>523.39</b>	<b>613.71</b>	<b>594.67</b>	<b>1017.66</b>	<b>990.87</b>	<b>746.22</b>	<b>732.72</b>	<b>683.65</b>		<b>320.99</b>	<b>391.32</b>	<b>356.96</b>	<b>486.52</b>
	MiniSplatting [16]	727.18	831.48	913.19	652.21	700.11	1032.53	962.47	679.40	683.06		312.32	347.06	347.31	418.42
	SEELE + MiniSplatting	<b>399.97</b>	<b>459.61</b>	<b>482.96</b>	<b>359.97</b>	<b>392.56</b>	<b>565.16</b>	<b>492.82</b>	<b>403.60</b>	<b>371.00</b>		<b>169.88</b>	<b>174.92</b>	<b>205.22</b>	<b>243.94</b>
	LightGaussian [15]	2008.94	1060.64	1291.92	1142.53	1782.13	1630.33	1928.39	1467.85	1488.80		582.87	816.55	851.42	1344.23
	SEELE + LightGaussian	<b>731.61</b>	<b>411.15</b>	<b>504.45</b>	<b>458.44</b>	<b>740.96</b>	<b>693.52</b>	<b>625.09</b>	<b>601.90</b>	<b>541.49</b>		<b>219.18</b>	<b>300.37</b>	<b>276.82</b>	<b>371.69</b>
Mem.↓ (MB)	3DGS [27]	1320.0	295.7	276.2	772.4	1305.1	410.5	352.0	942.9	720.8		257.5	604.3	543.3	736.6
	SEELE + 3DGS	<b>706.9</b>	<b>145.4</b>	<b>166.6</b>	<b>382.3</b>	<b>728.3</b>	<b>295.8</b>	<b>204.3</b>	<b>433.9</b>	<b>364.2</b>		<b>135.5</b>	<b>279.6</b>	<b>387.0</b>	<b>414.3</b>
	MiniSplatting [16]	157.6	147.0	130.7	142.4	176.0	142.3	121.5	157.8	136.7		85.0	81.5	117.4	192.3
	SEELE + MiniSplatting	<b>107.8</b>	<b>91.7</b>	<b>106.9</b>	<b>95.7</b>	<b>126.1</b>	<b>122.4</b>	<b>98.0</b>	<b>114.8</b>	<b>95.4</b>		<b>62.6</b>	<b>57.7</b>	<b>104.9</b>	<b>154.3</b>
	LightGaussian [15]	106.7	24.1	23.8	64.2	94.4	34.6	28.3	89.4	68.7		23.5	44.2	38.9	66.0
	SEELE + LightGaussian	<b>65.3</b>	<b>15.0</b>	<b>19.4</b>	<b>37.2</b>	<b>66.3</b>	<b>30.6</b>	<b>21.9</b>	<b>55.3</b>	<b>41.2</b>		<b>14.7</b>	<b>26.6</b>	<b>33.6</b>	<b>49.2</b>

## 7.4. Sensitivity Study

**Number of Clusters.** Fig. 8 shows how rendering quality and performance vary with two key hyperparameters, the number of clusters and the number of neighboring clusters during rendering ( $M$ ), in Sec. 4. Performance numbers are normalized to our default setting of 24 clusters with 4 neighbors (including itself). As the number of neighboring clusters increases, speedup decreases, while accuracy initially improves. However, too many clusters, e.g., 8 clusters

with 8 neighbors, degrades accuracy. This degradation is because each Gaussian is responsible for too many view directions, negatively impacting rendering quality.

Fig. 12 shows example results from our sensitivity study on rendering quality and performance to the number of clusters and cluster neighbors. All results are generated by partitioning the entire scene with 24 clusters while varying the number of neighboring clusters. We find that most artifacts come from uncovered regions, primarily due to an insuf-

Table 3. The ablation study of 3DGS dissects our contributions. +Opti. refers to the code optimization in Sec. 7.1, +HP represents the *hybrid preprocessing* in Sec. 4, +CR represents the *contribution-aware rasterization* in Sec. 5, and SEELE is our full-fledged algorithm.

Dataset	Mip-NeRF360						Tanks&Temples						Deep Blending					
	Quality			Efficiency			Quality			Efficiency			Quality			Efficiency		
Metrics	PSNR $\uparrow$	SSIM $\uparrow$	LPIPS $\downarrow$	FPS $\uparrow$	#Inst.(10 <sup>6</sup> ) $\downarrow$	Mem.(MB) $\downarrow$	PSNR $\uparrow$	SSIM $\uparrow$	LPIPS $\downarrow$	FPS $\uparrow$	#Inst.(10 <sup>6</sup> ) $\downarrow$	Mem.(MB) $\downarrow$	PSNR $\uparrow$	SSIM $\uparrow$	LPIPS $\downarrow$	FPS $\uparrow$	#Inst.(10 <sup>6</sup> ) $\downarrow$	Mem.(MB) $\downarrow$
3DGS [27]	27.46	0.812	0.223	20.79	2168.68	710.6	23.75	0.848	0.176	41.97	1034.37	430.9	29.59	0.902	0.244	23.94	1645.11	639.9
3DGS+Opti.	27.46	0.812	0.223	21.75	1945.88	710.6	23.75	0.847	0.176	45.96	923.51	430.9	29.59	0.902	0.244	29.60	1485.44	639.9
3DGS+Opti.+HP	27.70	0.814	0.219	46.15	814.74	380.9	24.05	0.852	0.171	118.61	374.63	207.6	29.74	0.903	0.242	81.73	<b>412.50</b>	400.6
3DGS+Opti.+CR	27.50	0.812	0.221	30.10	1574.92	710.6	23.70	0.848	0.173	57.03	763.83	430.9	29.70	0.902	0.242	38.79	1156.46	639.9
SEELE + 3DGS	<b>27.72</b>	<b>0.814</b>	<b>0.217</b>	<b>59.67</b>	<b>778.25</b>	<b>380.9</b>	<b>24.02</b>	<b>0.852</b>	<b>0.168</b>	<b>127.80</b>	<b>356.15</b>	<b>207.6</b>	<b>29.79</b>	<b>0.903</b>	<b>0.240</b>	<b>86.58</b>	421.74	<b>400.6</b>
MiniSplatting	27.23	0.814	0.222	71.31	797.96	145.7	23.18	0.837	0.187	143.27	329.69	83.3	30.04	0.908	0.243	120.01	382.86	154.9
MiniSplatting+Opti.	27.24	0.814	0.223	83.16	669.35	145.7	23.19	0.837	0.188	162.29	277.99	83.3	30.03	0.908	0.243	146.24	302.23	154.9
MiniSplatting+Opti.+HP	27.70	0.823	0.213	102.95	<b>421.39</b>	106.5	23.75	0.846	0.181	210.31	<b>169.92</b>	60.1	30.02	0.908	0.242	155.67	<b>197.19</b>	129.6
MiniSplatting+Opti.+CR	27.22	0.814	0.222	100.14	608.65	145.7	23.18	0.837	0.186	192.47	257.53	83.3	30.04	0.908	0.243	169.15	295.35	154.9
SEELE + MiniSplatting	<b>27.70</b>	<b>0.822</b>	<b>0.212</b>	<b>131.62</b>	<b>436.41</b>	<b>106.5</b>	<b>23.74</b>	<b>0.846</b>	<b>0.179</b>	<b>268.03</b>	<b>172.40</b>	<b>60.1</b>	<b>30.02</b>	<b>0.908</b>	<b>0.242</b>	<b>200.62</b>	224.58	<b>129.6</b>
LightGaussian	27.44	0.807	0.235	30.89	1533.50	59.4	23.82	0.842	0.189	65.60	699.71	33.8	29.74	0.901	0.250	43.17	1097.82	52.4
LightGaussian+Opti.	27.42	0.807	0.236	34.48	1365.02	59.4	23.83	0.841	0.190	72.46	620.48	33.8	29.72	0.900	0.251	48.41	980.20	52.4
LightGaussian+Opti.+HP	27.64	0.811	0.230	70.55	600.20	39.1	24.04	0.847	0.182	172.00	261.86	20.7	29.74	0.901	0.250	126.65	<b>306.88</b>	41.4
LightGaussian+Opti.+CR	27.43	0.807	0.235	40.15	1127.65	59.4	23.81	0.842	0.188	85.36	525.97	33.8	29.74	0.901	0.250	58.59	783.34	52.4
SEELE + LightGaussian	<b>27.56</b>	<b>0.810</b>	<b>0.229</b>	<b>76.36</b>	<b>589.85</b>	<b>39.1</b>	<b>23.91</b>	<b>0.846</b>	<b>0.181</b>	<b>183.86</b>	<b>259.78</b>	<b>20.7</b>	<b>29.73</b>	<b>0.900</b>	<b>0.249</b>	<b>131.16</b>	324.25	<b>41.4</b>

Table 4. Quality and performance comparison on 3DGS with and without integrated fine-tuning on 3DGS.

Dataset Metric	Mip-NeRF360					
	PSNR $\uparrow$	SSIM $\uparrow$	LPIPS $\downarrow$	FPS $\uparrow$	#Inst.(10 <sup>6</sup> ) $\downarrow$	Mem. (MB) $\downarrow$
w/o Fine-tuning	27.48	0.812	0.221	59.72	768.76	380.9
w/ Fine-tuning	27.72	0.814	0.217	59.67	778.25	380.9

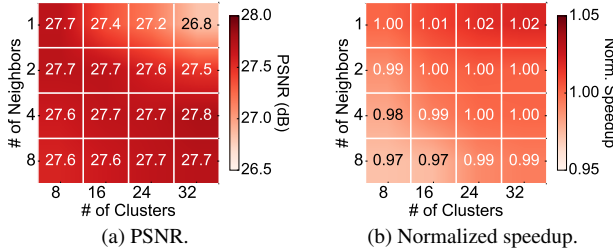


Fig. 8. Sensitivity of rendering quality and performance to the number of clusters and cluster neighbors in Sec. 4.

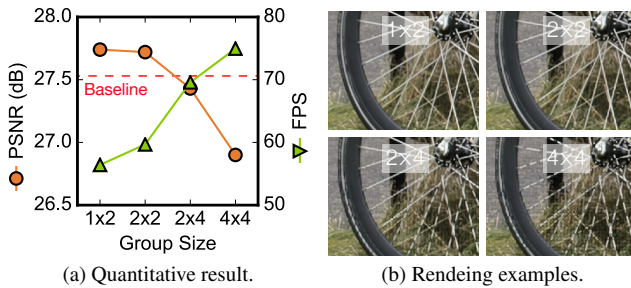


Fig. 9. Sensitivity of rendering quality and performance to the pixel group size using Mip-NeRF360 [13] in Sec. 5. The red dash line in Fig. 9a shows the baseline accuracy.

ficient number of neighboring clusters. Please see details highlighted in red bounding boxes. The lack of neighboring clusters results in black ghosting shadows (Fig. 12).

**Pixel Group.** Fig. 9 illustrates the sensitivity of both

the rendering quality and performance to the pixel group size using Mip-NeRF360 [13], as defined in Sec. 5. Other datasets show a similar trend. As the pixel group size increases, rendering quality initially decreases slightly, but the drop becomes more significant once the group size exceeds  $2 \times 4$ . We also present examples of rendered images with different group sizes in Fig. 9b. As the group size increases to  $2 \times 4$ , artifacts begin to appear in the high-frequency regions. On the performance side, speedup increases sub-linearly at first, but it almost plateaus once the group size reaches  $2 \times 4$ . Thus, we ultimately select  $2 \times 2$ .

Fig. 13 presents the qualitative results analyzing the sensitivity of both rendering quality and performance to pixel group size. One potential limitation of this technique is that as the window size increases, artifacts such as aliasing may appear in the rendered images. For instance, when the window size reaches  $4 \times 4$ , noticeable aliasing effects can be observed, as shown on the right side of Fig. 13.

## 8. Limination and Discussion

**Limitation.** This paper presents SEELE, a unified framework that achieves speedup across GPUs. Nevertheless, we acknowledge several limitations of this work:

- *Scene-Specific Configuration in Hybrid Preprocessing:* In this work, we adopt a uniform configuration for clustering in hybrid preprocessing. We believe that scene-specific configurations could further enhance rendering performance and quality. However, manually tuning the number of clusters and neighboring clusters is cumbersome with a human in the loop. An interesting future work would be designing an automatic algorithm to optimize these parameters for each scene.
- *Aliasing in Contribution-Aware Rasterization:* We observe that increasing the window size to  $4 \times 4$  introduces aliasing artifacts in high-frequency regions when applying *contribution-aware rasterization*. While our current approach balances speedup and quality, further investiga-



tion is needed to develop techniques that mitigate aliasing while maintaining efficiency.

Meanwhile, we acknowledge several works that leverage GPU fixed-function units to accelerate alpha blending using GPU RT Core [38], GPU raster [12], or WebGL [11]. Our approach is orthogonal to these methods, and we are excited to explore how our techniques can be integrated with these optimizations to further enhance rendering performance.

**Looking Forward.** Recent neural rendering has changed the landscape of real-time rendering. Gaussian splatting emerges as a new rendering primitive that offers unprecedented realism using the conventional rasterization pipeline. This paper proposes two principled and GPU-oriented optimizations that drastically improve the general Gaussian splatting pipelines by understanding and leveraging the GPUs’ characteristics. We believe this work could be the first step to understanding the fundamental limitations of GPUs in supporting Gaussian splatting. The result would be valuable for rethinking brand-new architectures tailored to this future technology.

## References

- [1] Geforce rtx 4090: Graphics cards for gaming. [1](#)
- [2] Nvidia a100 tensor core gpu: Unprecedented acceleration at every scale. [1](#)
- [3] Nvidia rtx a6000. [7](#)
- [4] Nvidia nsight compute. [8](#)
- [5] Nvidia jetson orin nx 16 gb, . [7](#)
- [6] Jetson orin for next-gen robotics, . [1, 3](#)
- [7] Meta Quest Pro specs. [2](#)
- [8] Qualcomm QCS8550/QCM8550 Processors. [1](#)
- [9] Apple Vision Pro screen refresh rate is up to 100Hz. [2](#)
- [10] Qualcomm Powers Next-Gen Spatial Computing With XR2 Gen 2 And AR1 Gen 1 Platforms. [1](#)
- [11] WebGL 3d gaussian splat viewer. GitHub, 2023. [11](#)
- [12] Fast gaussian rasterization. GitHub, 2024. [11](#)
- [13] Jonathan T Barron, Ben Mildenhall, Matthew Tancik, Peter Hedman, Ricardo Martin-Brualla, and Pratul P Srinivasan. Mip-nerf: A multiscale representation for anti-aliasing neural radiance fields. In *Proceedings of the IEEE/CVF International Conference on Computer Vision*, pages 5855–5864, 2021. [1, 5, 7, 10](#)
- [14] Zhiqin Chen, Thomas Funkhouser, Peter Hedman, and Andrea Tagliasacchi. Mobilenerf: Exploiting the polygon rasterization pipeline for efficient neural field rendering on mobile architectures. In *Proceedings of the IEEE/CVF Conference on Computer Vision and Pattern Recognition*, pages 16569–16578, 2023. [1](#)
- [15] Zhiwen Fan, Kevin Wang, Kairun Wen, Zehao Zhu, Dejia Xu, and Zhangyang Wang. Lightgaussian: Unbounded 3d gaussian compression with 15x reduction and 200+ fps. *arXiv preprint arXiv:2311.17245*, 2023. [1, 2, 3, 7, 8, 9](#)
- [16] Guangchi Fang and Bing Wang. Mini-splatting: Representing scenes with a constrained number of gaussians. *arXiv preprint arXiv:2403.14166*, 2024. [1, 2, 3, 7, 8, 9](#)
- [17] Guofeng Feng, Siyan Chen, Rong Fu, Zimu Liao, Yi Wang, Tao Liu, Zhilin Pei, Hengjie Li, Xingcheng Zhang, and Bo Dai. Flashgs: Efficient 3d gaussian splatting for large-scale and high-resolution rendering. *arXiv preprint arXiv:2408.07967*, 2024. [3](#)
- [18] Yu Feng, Weikai Lin, Zihan Liu, Jingwen Leng, Minyi Guo, Han Zhao, Xiaofeng Hou, Jieru Zhao, and Yuhao Zhu. Potamoi: Accelerating neural rendering via a unified streaming architecture. *ACM Transactions on Architecture and Code Optimization*, 21(4):1–25, 2024. [3](#)
- [19] Yu Feng, Zihan Liu, Jingwen Leng, Minyi Guo, and Yuhao Zhu. Cicero: Addressing algorithmic and architectural bottlenecks in neural rendering by radiance warping and memory optimizations. *arXiv preprint arXiv:2404.11852*, 2024. [5](#)
- [20] Sharath Girish, Kamal Gupta, and Abhinav Shrivastava. Eagles: Efficient accelerated 3d gaussians with lightweight encodings. In *European Conference on Computer Vision*, pages 54–71. Springer, 2024. [1, 2, 3, 8](#)
- [21] Stefan Gottschalk, Ming C Lin, and Dinesh Manocha. Obbtree: A hierarchical structure for rapid interference detection. In *Proceedings of the 23rd annual conference on Computer graphics and interactive techniques*, pages 171–180, 1996. [3](#)
- [22] Hao Gui, Lin Hu, Rui Chen, Mingxiao Huang, Yuxin Yin, Jin Yang, and Yong Wu. Balanced 3dgs: Gaussian-wise parallelism rendering with fine-grained tiling. *arXiv preprint arXiv:2412.17378*, 2024. [3](#)
- [23] Peter Hedman, Julien Philip, True Price, Jan-Michael Frahm, George Drettakis, and Gabriel Brostow. Deep blending for free-viewpoint image-based rendering. *ACM Transactions on Graphics (TOG)*, 37(6):1–15, 2018. [1, 7](#)
- [24] Peter Hedman, Pratul P Srinivasan, Ben Mildenhall, Jonathan T Barron, and Paul Debevec. Baking neural radiance fields for real-time view synthesis. In *Proceedings of the IEEE/CVF International Conference on Computer Vision*, pages 5875–5884, 2021. [1](#)
- [25] Xueshi Hou and Sujit Dey. Motion prediction and pre-rendering at the edge to enable ultra-low latency mobile 6dof experiences. *IEEE Open Journal of the Communications Society*, 1:1674–1690, 2020. [5](#)
- [26] Tao Hu, Shu Liu, Yilun Chen, Tiancheng Shen, and Jiaya Jia. Efficientnerf efficient neural radiance fields. In *Proceedings of the IEEE/CVF Conference on Computer Vision and Pattern Recognition*, pages 12902–12911, 2022. [1](#)
- [27] Bernhard Kerbl, Georgios Kopanas, Thomas Leimkühler, and George Drettakis. 3d gaussian splatting for real-time radiance field rendering. *ACM Transactions on Graphics*, 42(4):1–14, 2023. [1, 7, 8, 9, 10](#)
- [28] Bernhard Kerbl, Andreas Meuleman, Georgios Kopanas, Michael Wimmer, Alexandre Lanvin, and George Drettakis. A hierarchical 3d gaussian representation for real-time rendering of very large datasets. *ACM Transactions on Graphics (TOG)*, 43(4):1–15, 2024. [1, 3](#)
- [29] James T Klosowski, Martin Held, Joseph SB Mitchell, Henry Sowizral, and Karel Zikan. Efficient collision detection using bounding volume hierarchies of k-dops. *IEEE transactions on Visualization and Computer Graphics*, 4(1):21–36, 1998. [3](#)

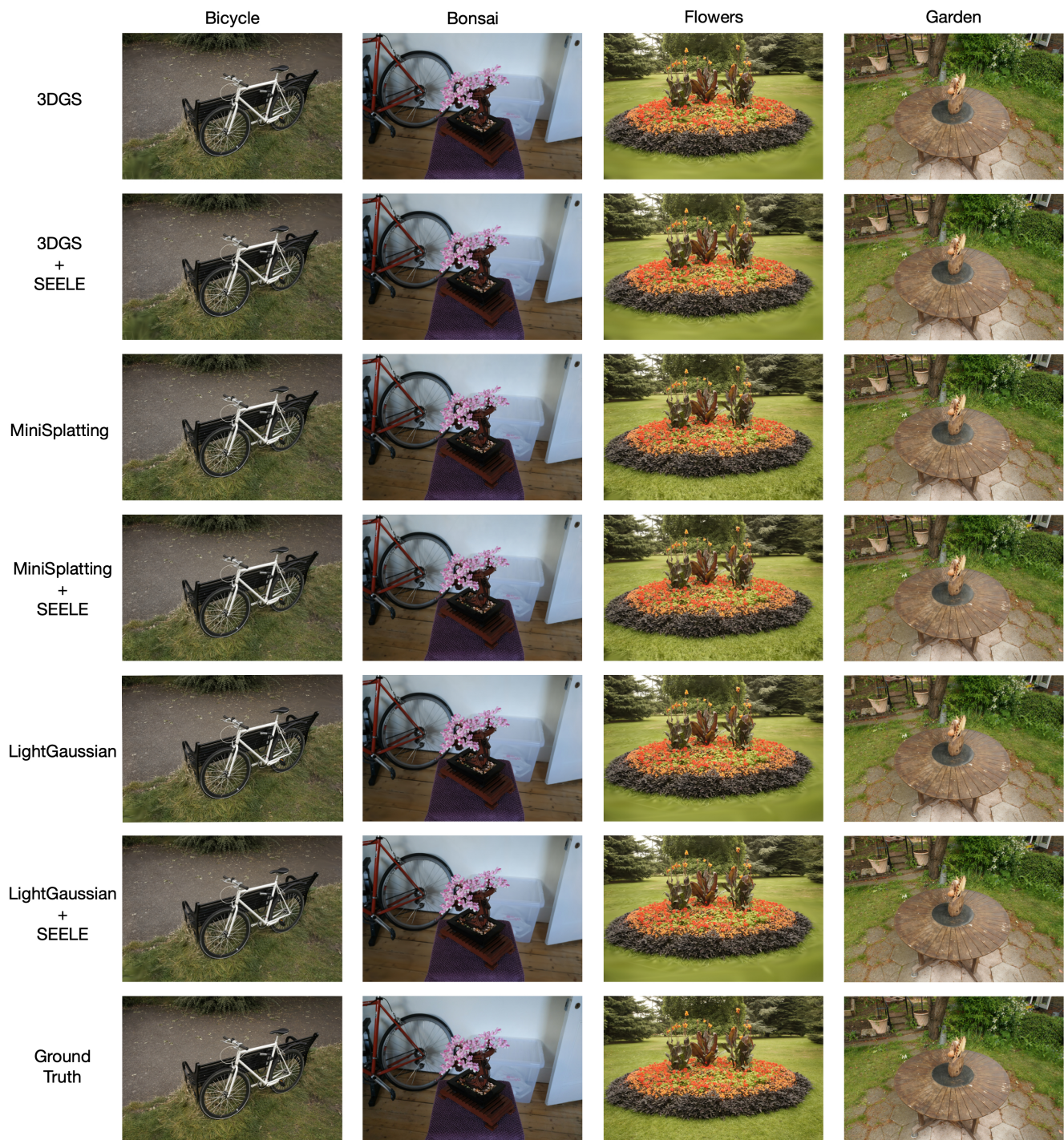


Fig. 10. Example figures of the overall comparison between SEELE and its corresponding baselines.

[30] Arno Knapitsch, Jaesik Park, Qian-Yi Zhou, and Vladlen Koltun. Tanks and temples: Benchmarking large-scale scene reconstruction. *ACM Transactions on Graphics*, 36(4), 2017. [1, 7](#)

[31] Junseo Lee, Seokwon Lee, Jungi Lee, Junyong Park, and Jae-

woong Sim. Gscore: Efficient radiance field rendering via architectural support for 3d gaussian splatting. In *Proceedings of the 29th ACM International Conference on Architectural Support for Programming Languages and Operating Systems, Volume 3*, pages 497–511, 2024. [3](#)



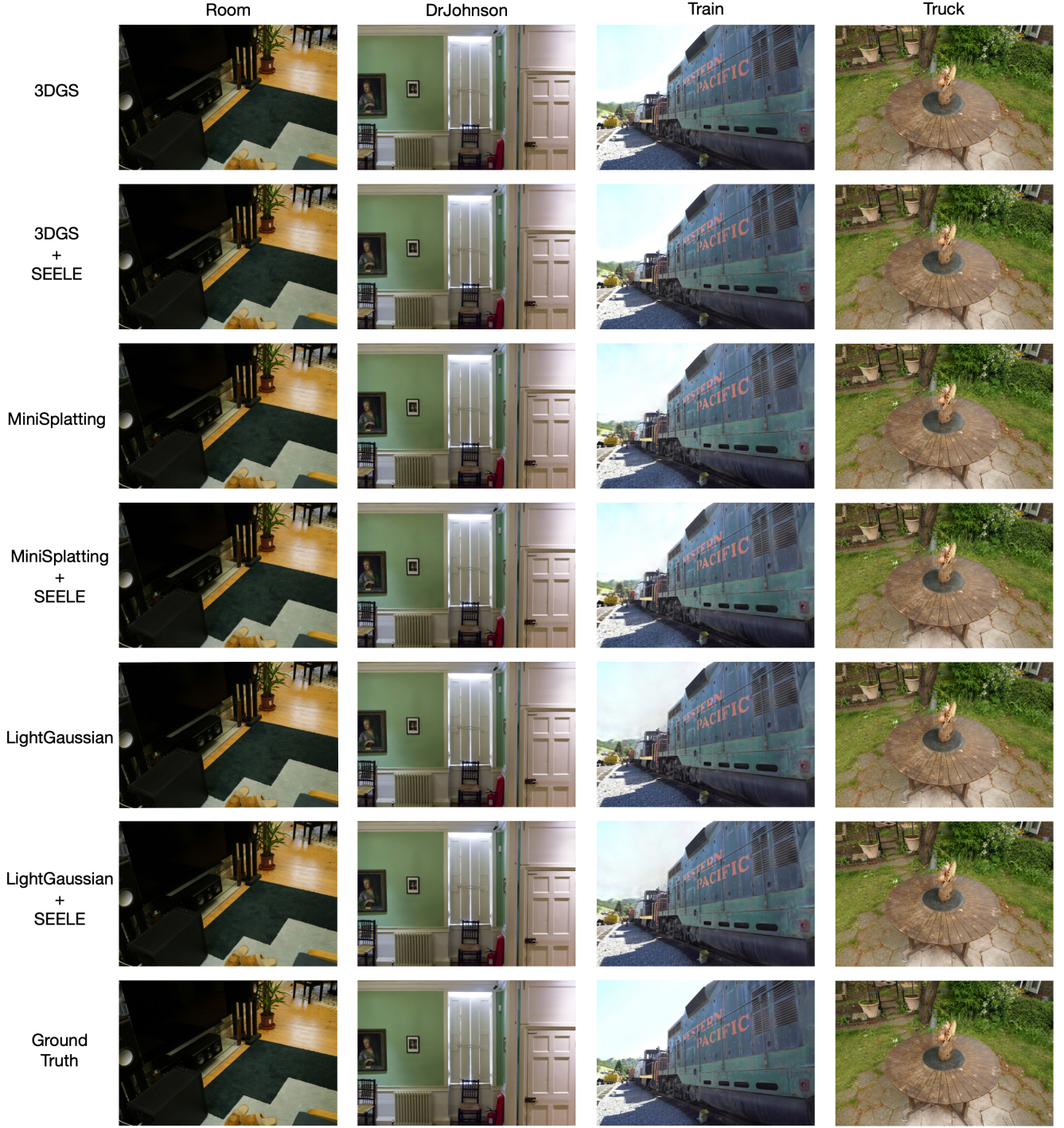


Fig. 11. More example figures of the overall comparison between SEELE and its corresponding baselines.

[32] Joo Chan Lee, Daniel Rho, Xiangyu Sun, Jong Hwan Ko, and Eunbyung Park. Compact 3d gaussian representation for radiance field. In *Proceedings of the IEEE/CVF Conference on Computer Vision and Pattern Recognition*, pages 21719–21728, 2024. [1](#), [2](#), [8](#)

[33] Weikai Lin, Yu Feng, and Yuhao Zhu. Rtgs: Enabling real-time gaussian splatting on mobile devices using efficiency-guided pruning and foveated rendering. *arXiv preprint arXiv:2407.00435*, 2024. [2](#)

[34] Weikai Lin, Yu Feng, and Yuhao Zhu. Metasapiens: Real-



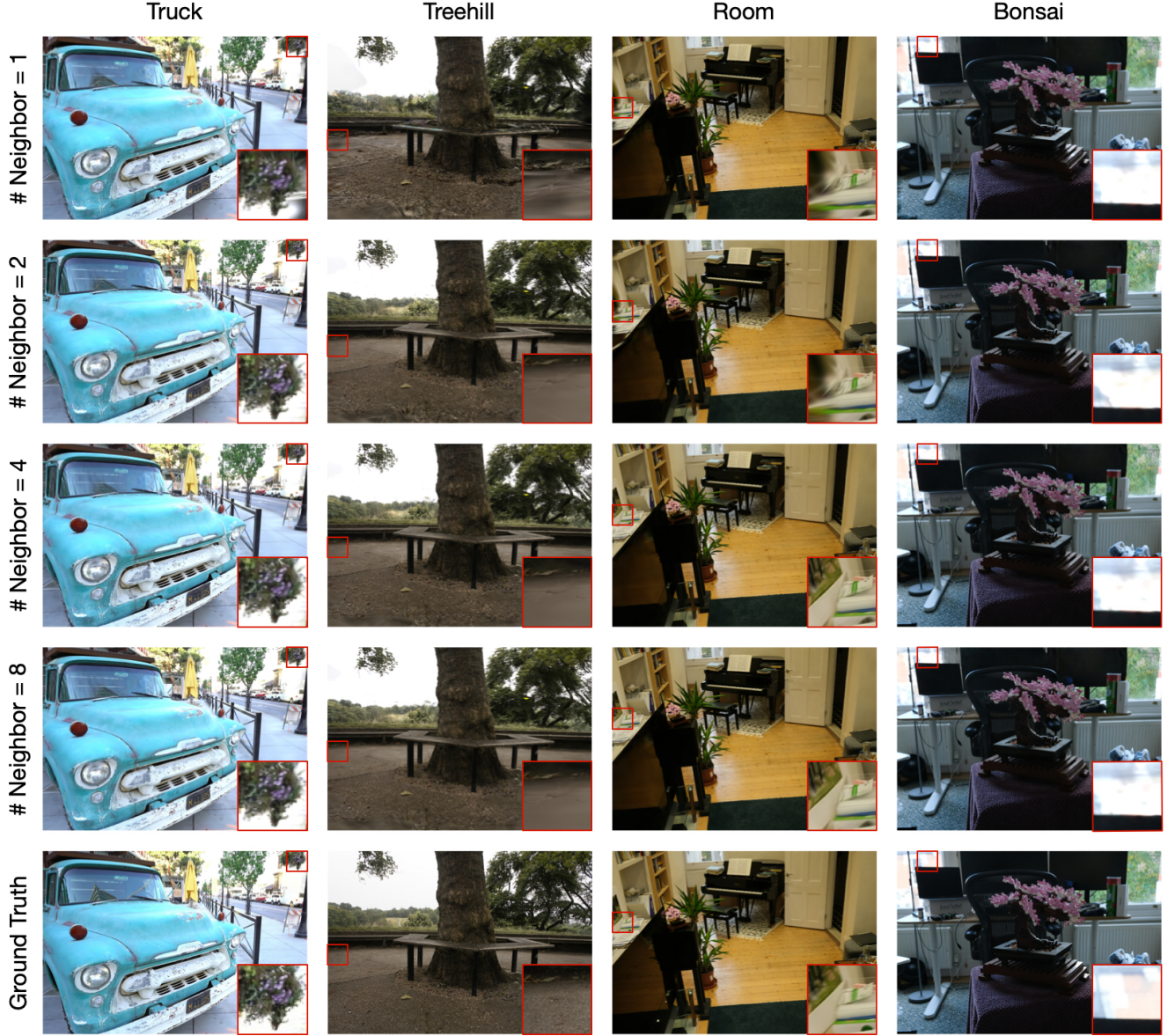


Fig. 12. Example results from our sensitivity study on rendering quality and performance to the number of clusters and cluster neighbors. All results are generated by partitioning the entire scene with 24 clusters while varying the number of neighboring clusters. We find that most artifacts come from uncovered regions, primarily due to an insufficient number of neighboring clusters. See red bounding boxes.

- time neural rendering with efficiency-aware pruning and accelerated foveated rendering. In *Proceedings of the 30th ACM International Conference on Architectural Support for Programming Languages and Operating Systems, Volume 1*, pages 669–682, 2025. 3
- [35] Yang Liu, Chuanchen Luo, Zhongkai Mao, Junran Peng, and Zhaoxiang Zhang. Citygaussian2: Efficient and geometrically accurate reconstruction for large-scale scenes. *arXiv preprint arXiv:2411.00771*, 2024. 1
- [36] Yang Liu, Chuanchen Luo, Lue Fan, Naiyan Wang, Junran Peng, and Zhaoxiang Zhang. Citygaussian: Real-time high-quality large-scale scene rendering with gaussians. In *European Conference on Computer Vision*, pages 265–282. Springer, 2025. 1
- [37] Saswat Subhajyoti Mallick, Rahul Goel, Bernhard Kerbl, Markus Steinberger, Francisco Vicente Carrasco, and Fernando De La Torre. Taming 3dgs: High-quality radiance fields with limited resources. In *SIGGRAPH Asia 2024 Conference Papers*, pages 1–11, 2024. 2, 3
- [38] Nicolas Moenne-Loccoz, Ashkan Mirzaei, Or Perel, Riccardo de Lutio, Janick Martinez Esturo, Gavriel State, Sanja Fidler, Nicholas Sharp, and Zan Gojcic. 3d gaussian ray tracing: Fast tracing of particle scenes. *ACM Transactions on Graphics (TOG)*, 43(6):1–19, 2024. 11



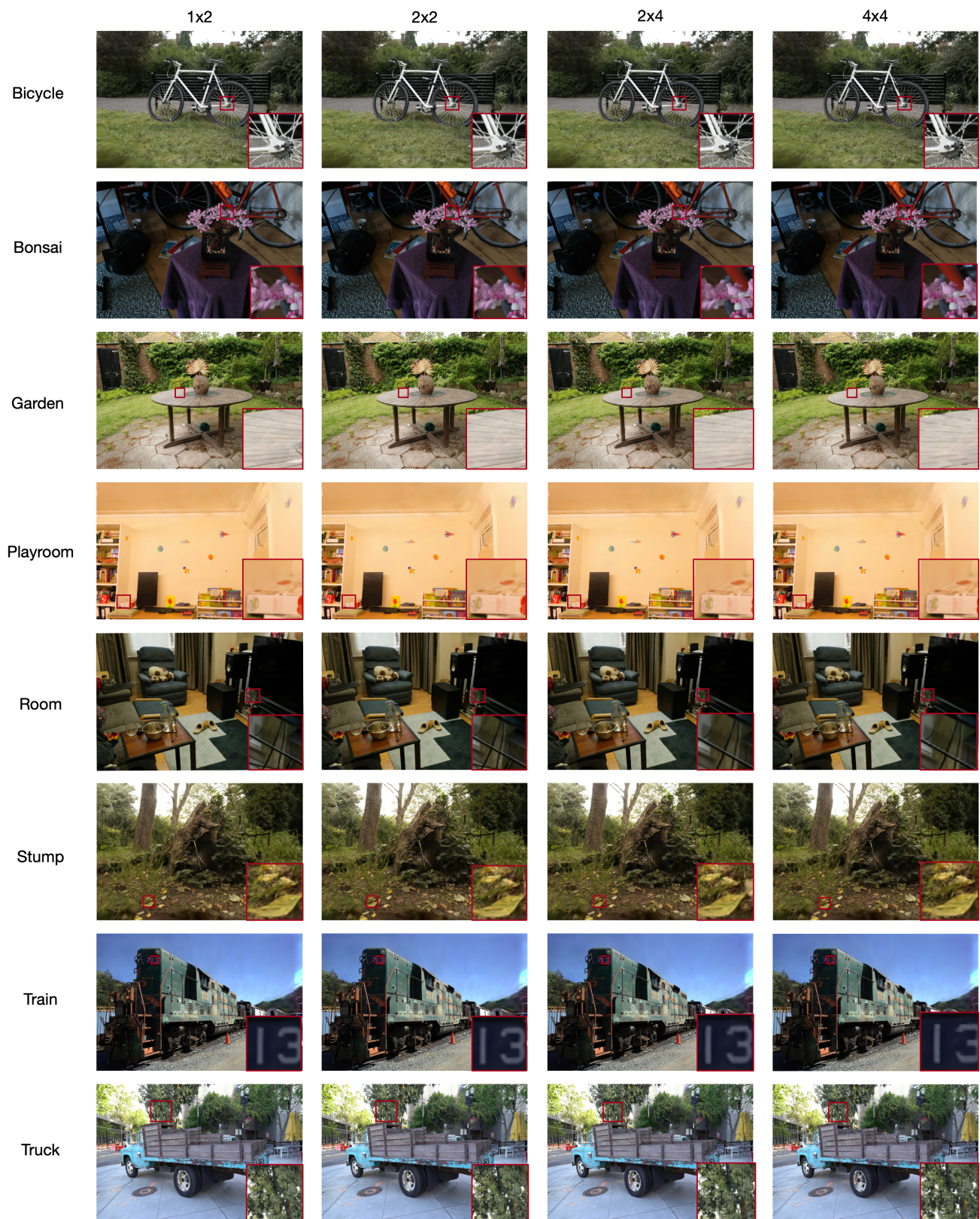


Fig. 13. Example results from the sensitivity study of rendering quality and performance to the pixel group size.

- [39] Michael Niemeyer, Fabian Manhardt, Marie-Julie Rakotsana, Michael Oechsle, Daniel Duckworth, Rama Gosula, Keisuke Tateno, John Bates, Dominik Kaeser, and Federico Tombari. Radsplat: Radiance field-informed gaussian splatting for robust real-time rendering with 900+ fps. *arXiv preprint arXiv:2403.13806*, 2024. [2](#)
- [40] Kerui Ren, Lihan Jiang, Tao Lu, Mulin Yu, Linning Xu, Zhangkai Ni, and Bo Dai. Octree-gs: Towards consistent real-time rendering with lod-structured 3d gaussians. *arXiv preprint arXiv:2403.17898*, 2024. [2](#), [3](#)
- [41] Sara Rojas, Jesus Zarzar, Juan C Pérez, Artsiom Sanakoyeu, Ali Thabet, Albert Pumarola, and Bernard Ghanem. Rend: Real-time rendering of nerfs across devices. In *Proceedings of the IEEE/CVF International Conference on Computer Vision*, pages 3632–3641, 2023. [1](#)
- [42] Matthew Tancik, Vincent Casser, Xincheng Yan, Sabeek Pradhan, Ben Mildenhall, Pratul P Srinivasan, Jonathan T Barron, and Henrik Kretschmar. Block-nerf: Scalable large scene neural view synthesis. In *Proceedings of the IEEE/CVF Conference on Computer Vision and Pattern Recognition*, pages 8248–8258, 2022. [1](#)
- [43] Jialin Wang, Rongkai Shi, Wenxuan Zheng, Weijie Xie, Dominic Kao, and Hai-Ning Liang. Effect of frame rate on user experience, performance, and simulator sickness in virtual reality. *IEEE Transactions on Visualization and Computer Graphics*, 29(5):2478–2488, 2023. [2](#), [8](#)
- [44] Xinzhe Wang, Ran Yi, and Lizhuang Ma. Adr-gaussian: Accelerating gaussian splatting with adaptive radius. In *SIGGRAPH Asia 2024 Conference Papers*, pages 1–10, 2024. [3](#), [8](#)
- [45] Matthias Zwicker, Hanspeter Pfister, Jeroen Van Baar, and Markus Gross. Ewa volume splatting. In *Proceedings Visualization, 2001. VIS'01.*, pages 29–538. IEEE, 2001. [3](#)